Journal of Power Sources 180 (2008) 433–439

Contents lists available at ScienceDirect

Journal of Power Sources

journal homepage: www.elsevier.com/locate/jpowsour

Oxidation resistance of novel ferritic stainless steels alloyed with titanium for SOFC interconnect applications

Paul D. Jablonski*, David E. Alman

National Energy Technology Laboratory, Process Development, 1450 Queen Avenue SW, Albany, OR 97321, USA

ARTICLE INFO

Article history:
Received 10 January 2008
Received in revised form 5 February 2008
Accepted 6 February 2008
Available online 16 February 2008

Keywords:
SOFC
Interconnect
Oxidation
Ferritic steel
Cr poisoning
Surface treatment

ABSTRACT

Chromia (Cr_2O_3) forming ferritic stainless steels are being developed for interconnect application in Solid Oxide Fuel Cells (SOFC). A problem with these alloys is that in the SOFC environment chrome in the surface oxide can evaporate and deposit on the electrochemically active sites within the fuel cell. This poisons and degrades the performance of the fuel cell. The development of steels that can form conductive outer protective oxide layers other than Cr_2O_3 or $(CrMn)_3O_4$ such as TiO_2 may be attractive for SOFC application. This study was undertaken to assess the oxidation behavior of ferritic stainless steel containing 1 weight percent (wt.%) Ti, in an effort to develop alloys that form protective outer TiO_2 scales. The effect of Cr content (6–22 wt.%) and the application of a Ce-based surface treatment on the oxidation behavior (at 800 °C in air + 3% H_2O) of the alloys was investigated. The alloys themselves failed to form an outer TiO_2 scale even though the large negative ΔG of this compound favors its formation over other species. It was found that in conjunction with the Ce-surface treatment, a continuous outer TiO_2 oxide layer could be formed on the alloys, and in fact the alloy with 12 wt.% Cr behaved in an identical manner as the alloy with 22 wt.% Cr.

Published by Elsevier B.V.

1. Introduction

Solid Oxide Fuel Cells (SOFC) are solid state energy conversion devices [1,2] converting a fuel such as H_2 or CO directly into electricity without combustion. In their simplest form they consist of an anode, a cathode and an electrolyte. A single cell can produce current density and voltage in the order of 1 A cm^{-2} and 1 V, respectively. In order to develop greater power output, multiple cells are grouped together. In planar SOFC they are simply stacked together with an "interconnect" separating each cell [2,3]. This interconnect acts as an air/fuel separator and is part of the electrical circuit. Lanthanum chromate is a good choice as an interconnect material for high temperature application (>900 °C), however it is quite expensive. The core goal of the Solid State Energy Conversion Alliance (SECA) is the development of SOFC with a factory cost of \$400 kW^{-1} h^{-1} or less [4–6]. One of the cost enabling developments over the past few years is oxide component materials capable of operating at lower temperatures such as 700–800 °C [7–12]. This lower temperature range has provided for the consideration of metallic materials for interconnect applications [12–18]. Metallic interconnects have several advantages: low cost, ease in manufacturing, and high conductivity. Most metals and alloys will oxidize under both the anode and cathode conditions within an SOFC, thus a chief requirement is that the base metal oxide scale must be electrically conductive since this constitutes the majority of the electrical resistance in a metallic interconnect. Common high temperature metal alloys form oxide scales that contain chrome, silicon and aluminum oxides among others. Under SOFC operating conditions chrome oxide is a semi-conductor while silicon and aluminum oxides are insulators. Several commercial alloys have been developed for SOFC applications such as Crofer 22 APU (ThyssenKrupp VDM), Hitachi ZMG 232 (Hitachi Metals) and Ebrite (Allegheny Ludlum) all of which form chromium-rich oxide scales under oxidizing conditions.

Many SOFC designs will operate at temperatures exceeding 700 °C. At these temperatures in the moist SOFC cathode environment, Cr_2O_3 (chromia) evaporates and deposits on electrochemically active sites at the cathode–electrolyte interface. This degrades the electrical performance of the SOFC [21–27]. The formation of an outer Cr–Mn spinel will reduce Cr evaporation, but will not prevent the Cr poisoning of the electrochemical reactions. Consequently, there has been considerable attention given to developing coatings which prevent Cr migration from the steel interconnects into the cathode [27–30]. Alternatively, the development of steels that can form conductive, protective oxide layers other than Cr_2O_3 may be attractive for interconnect application. For example, TiO_2 may have electrical properties that are attractive for interconnect application [17–20]. This study was conceived to explore steels that could form outer protective TiO_2 scales during oxidation. Further, the effect of alloy Cr content and a reactive

* Corresponding author. Tel.: +1 541 967 5982; fax: +1 541 967 5958.
E-mail address: paul.jablonski@netl.doe.gov (P.D. Jablonski).

0378-7753/$ – see front matter. Published by Elsevier B.V.
doi:10.1016/j.jpowsour.2008.02.010

element surface treatment [31–33] on the oxidation of the experimental (Fe–Cr–1Ti–0.5Mn) alloys was investigated.

2. Experimental techniques

2.1. Alloy design and manufacture

Experimental alloy formulation was first evaluated theoretically with the use of Thermo-Calc (version r) and the TcFe5 database. High purity starting materials were used to formulate the series of alloys shown in Table 1. Approximately 6800 g of high purity raw materials was induction melted under inert gas and poured into a cylindrical mold for each alloy. These cylindrical ingots were machined and subsequently homogenization heat treated at 1150 °C/12 h/FC in vacuum. The homogenized ingots were bagged in protective stainless steel foil pouches and preheated to 900 °C for 3 h prior to fabrication. Hot working consisted of forging and rolling to fabricate the round ingot into a slab shape and ultimately form a strip product. These strips were hot worked to a thickness of 3 mm. Subsequently, these strips were conditioned to remove oxidation products and any residual surface defects prior to cold rolling. Each alloy was subsequently cold rolled to approximately 1 mm thickness.

2.2. Alloy testing and evaluation

Oxidation test coupons were cut from each of the alloys with the dimensions of approximately 12 mm × 24 mm × thickness and polished through 600 grit prior to testing. Some samples were drilled with a 3 mm diameter hole near one end to provide for hanging from a quartz rack while others were stood upright inside alumina crucibles. Further, some duplicate samples were surface treated with cerium oxide [31–33] before testing. Prior to oxidation testing the starting weights and physical dimensions of the coupons were measured and recorded. Oxidation tests were conducted at 800 °C in moist air. The moist air was generated by bubbling commercial purity dry air through two glass columns (2.54 cm in diameter by 120 cm in height) filled with distilled water just ahead of the furnace entrance. This was intended to generate air saturated with 3% H_2O, the maximum amount of moisture dissolvable in air at ambient conditions. After a predetermined time interval, the coupons were removed from the heated furnace, cooled and the weight of each coupon was measured and recorded. The samples were then reinserted into the heated furnace for the next cycle. Oxide scale surfaces were examined by standard X-ray diffraction (XRD) and scanning electron microscopy (SEM) techniques. Chemistries of the oxidized surfaces were determined by energy dispersive X-ray analysis (EDX). Oxidized coupons were also sectioned and polished via standard metallographic procedures to view the scales in cross section. These were analyzed by SEM with WDX analysis using in situ standards for metal and oxide scale chemistry.

Table 1
The design chemistries (weight percent) for the experimental series of alloys are found in the table below

	F7	F8	F9	F10	F11
Fe	Bal.	Bal.	Bal.	Bal.	Bal.
Cr	6	9	12	18	22
Ti	1	1	1	1	1
Al	0	0	0	0	0
Si	0	0	0	0	0
Mn	0.5	0.5	0.5	0.5	0.5
C	0	0	0	0	0

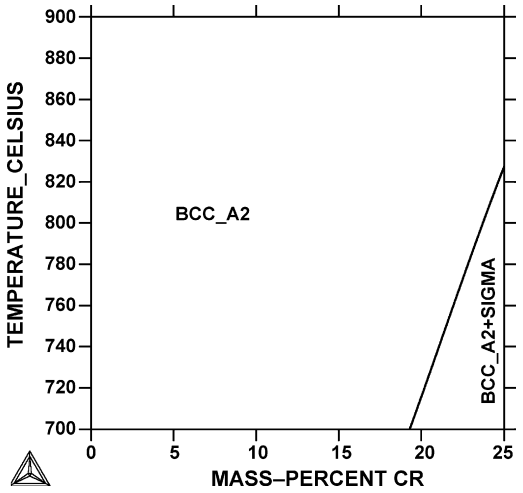

Fig. 1. Phases calculated to be present in an Fe–1Si–0.5Mn × Cr alloy (Thermo-Calc Classic version r used along with TcFe5 database).

3. Results

3.1. Alloy phases and chemistry

Thermo-Calc showed that all of the experimental alloys are expected to be single phase at the test conditions, similar to a simple ferritic stainless steel containing Si rather than Ti. However, it was observed that with high Cr and at lower temperatures (>22Cr and <800 °C) Sigma phase is predicted in the simple Si containing ferritic alloy (typical of many commercial ferritic stainless steels) while Laves phase is predicted in the experimental Ti containing alloy (Figs. 1 and 2). The possibility of Laves phase formation was not considered to be undesirable in these alloys. In fact, some researchers [34–36] are considering Laves phase as a way to tie up residual Si for a cost effective way of dealing with undesirable SiO_2 formation in ferritic alloy interconnects. However, is not a consideration in the present experimental alloys since they contain Ti but no Si. Furthermore, the experimental alloys were single phase under the test conditions.

The measured chemistry of the experimental alloys is found in Table 2. Good correlation was observed between the actual alloy composition and target composition. Furthermore, the alloys contained very low levels of “tramp” or undesirable elements. A

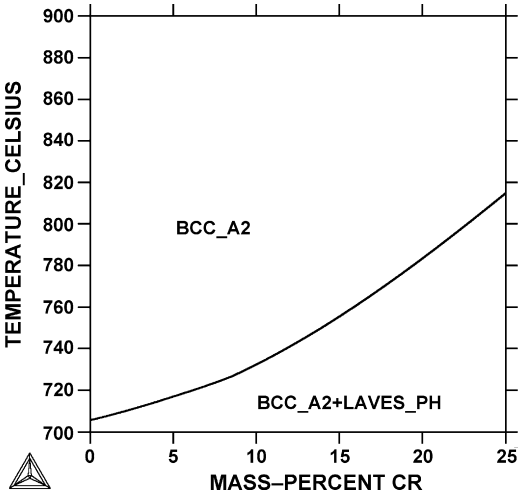

Fig. 2. Phases calculated to be present in an Fe–1Ti–0.5Mn × Cr alloy (Thermo-Calc Classic version r used along with TcFe5 database).

Table 2
The measured chemistries (weight percent) for the experimental series of alloys are found in the table below

	Fe	Mn	Cr	Si	Al	Ti	O	N	C	S
F7	Bal.	0.52	6.10	<0.010	0.037	1.00	0.002	0.0002	0.0053	0.0036
F8	Bal.	0.53	9.12	<0.010	0.042	1.00	0.001	0.0001	0.0048	0.0039
F9	Bal.	0.49	12.11	<0.010	0.041	1.03	0.001	0.0001	0.0090	0.0027
F10	Bal.	0.50	18.04	<0.010	0.035	1.01	0.002	0.0001	0.0037	0.0085
F11	Bal.	0.49	22.01	<0.010	0.028	1.01	0.003	0.0002	0.0095	0.0082

Metals were determined by XRF with a Rigaku ZSX Primus II, carbon and sulfur were determined with a LECO CS244 and oxygen and nitrogen were determined with a LECO CT436 all using certified standards.

Table 3
The phases identified by X-ray diffraction on the oxide scales formed on the specimen surfaces after 2000 h exposure at 800 °C in moist air

Alloy	Cr content (wt.%)	w/o Treatment	With Ce-surface treatment
F7	6	$FeFe_2O_4$ (magnetite) $FeTiO_3$	Fe_2O_3
F8	9	Fe_2O_3	Fe_2O_3; CeO_2; TiO_2; Spinel $(MnFeTi)_xO_y$
F9	12	Fe_2O_3	TiO_2; $Cr_{1.3}Fe_{0.7}O_3$; $MnFe_2O_4$; CeO_2
F10	18	$CrMn_{1.5}O_4$; $Cr_{1.3}Fe_{0.7}O_3$; TiO_2; Fe_2O_3	TiO_2; $Cr_{1.3}Fe_{0.7}O_3$; $MnFe_2O_4$; CeO_2;
F11	22	TiO_2; $Cr_{1.3}Fe_{0.7}O_3$; $CrMn_{1.5}O_4$; Fe_2O_3	TiO_2; $Cr_{1.3}Fe_{0.7}O_3$; $CrMn_{1.5}O_4$; CeO_2

low level of Si and Al is important for SOFC interconnect application as these elements form internal non-conductive Al_2O_3 and SiO_2 during oxidation, which will significantly degrade the electrical performance of an SOFC [33]. All of the alloys fabricated with ease by both hot and cold working into 1 mm thick sheet.

3.2. Oxidation testing results

Fig. 3 shows the influence of Cr content on the oxidation behavior of the experimental Fe–Cr–1Ti–0.5Mn alloys. The mass gain for the 6 and 9 wt.% Cr alloys was extremely rapid and could not be presented on the scale associated with Fig. 3. Testing of the low Cr alloys was discontinued after only 96 h of exposure, while the 12–22Cr alloys were tested out to 2000 h. The specific mass gain after 2000 h of oxidation was 55, 8 and 3 mg cm^{-2} for the 12, 18 and 22Cr alloys, respectively. These results indicate the benefit of increasing Cr content on oxidation resistance, but showed no beneficial impact of adding Ti to the base alloy. However, in the cerium surface treated condition the 12, 18 and 22 wt.% Cr experimental alloys (F9, F10, and F11) all had essentially equivalent mass gains, which were about half the mass gain of the untreated 22 wt.% Cr alloy (1.5 mg cm^{-2}). This is more clearly illustrated in Fig. 4, where the specific mass change is plotted for the experimental alloys as a function of Cr content, with and without the cerium surface treatment. In the untreated condition, the oxidation rate decreased significantly with increasing Cr content. However, no such strong dependence on Cr level was observed in the cerium surface treated condition.

The X-ray diffraction analysis of the scales is presented in Table 3. In the untreated condition, predominantly iron-rich oxides such as Fe_2O_3 formed on alloys with less than 12 wt.% Cr. Mixed oxides containing Cr and Mn or Fe formed on the alloys with 18 and 22 wt.% Cr. In both alloys, TiO_2 was also observed in the XRD scans. With the Ce-surface treatment, the mixed oxides and TiO_2 were found to form on alloys with lower Cr contents. Indeed, the Ce-surface treated 12, 18 and 22 wt.% Cr alloys have essentially identical oxide scales by XRD analysis, consistent with their similar mass gains during oxidation (Figs. 3 and 4). The remainder of this section will concentrate on further analysis comparing the experimental alloys with titanium and 12, 18 and 22 wt.% Cr.

The oxidized surface of the untreated experimental alloy containing 12 wt.% Cr is shown in Fig. 5. The scale was cracked and protruding whiskers were observed on the outer surface. The surface scale chemistry was determined to be iron rich by EDX which agrees well with the XRD determined structure of Fe_2O_3. The oxidized surface of the cerium treated experimental alloy containing 12 wt.% Cr is shown in Fig. 6. A uniform fine grained crystalline structure was observed. The chemistry of the scale at the surface

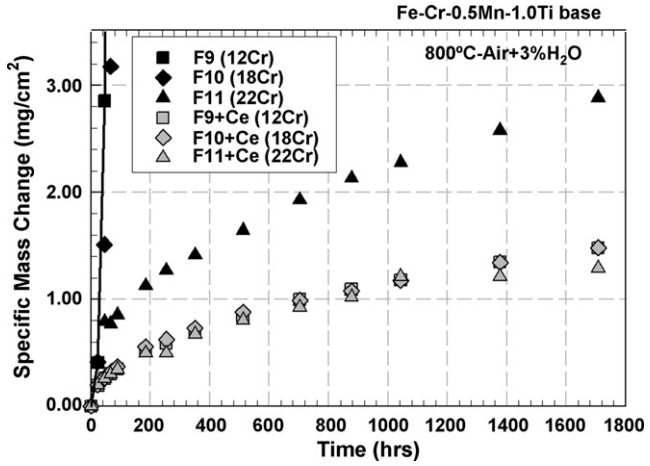

Fig. 3. Specific mass change as a function of exposure time is shown in the plot above. The bold symbols are the base materials while the grey symbols have been surface treated with cerium (see text for details).

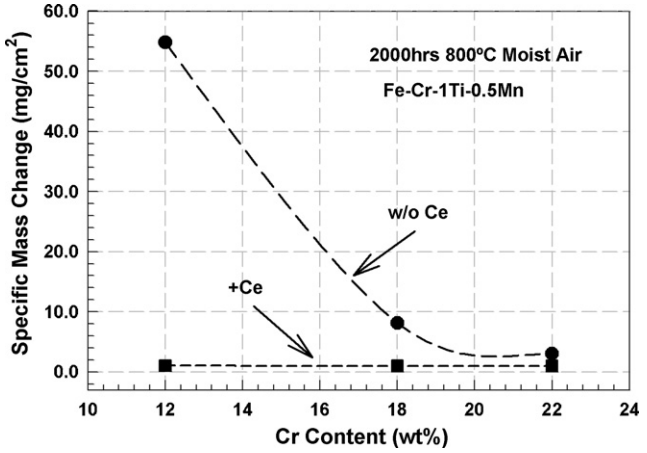

Fig. 4. Specific mass change as a function of chrome content is shown in the plot above for both the as-produced alloys (w/o Ce) and those in the surface treated condition (+Ce).

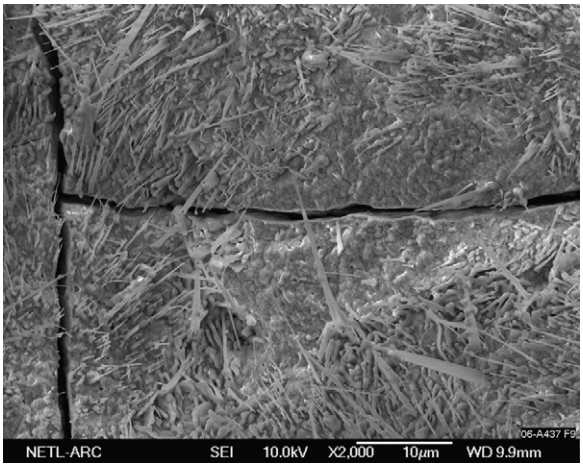

Fig. 5. An SEM micrograph of the oxide surface that formed on the F9 alloy (12Cr) after 2000 h exposure at 800 °C in moist air. Note that the scale is cracked and has oxide whiskers growing from the surface.

was determined to be titanium rich, which agrees with the XRD determined structure of TiO_2.

Figs. 7 and 8 contain SEM micrographs of cross sections of the oxide scales that formed on the experimental alloy with 12 wt.% Cr in the untreated and Ce treated conditions, respectively. Note the drastically different magnifications of the images and scale thicknesses. In the case of the untreated specimen (Fig. 7), a very complex multi-layered scale was observed that is predominantly Fe rich in the outer layers and predominantly Cr rich in the inner layers. Substantial titanium was found only in the oxide layers closest to the base alloy. In the case of the Ce treated specimen, an overgrowth of Ti-rich oxide was observed above the residual Ce–Ox particles. The WDX chemistry of this layer was $Ti_{40}O_{58}$, suggesting that it is likely non-stoichiometric TiO_2 that is forming as the outer layer. Chrome–manganese-rich oxides containing titanium were observed both under the Ti-rich layer and under the residual cerium oxide particles. A Cr-rich scale was observed at the oxide/metal interface. Some discrete internal oxidation (titanium rich) was also observed.

The oxidized surface of the untreated experimental alloy with 22 wt.% Cr is shown in Fig. 9. The scale was found to be quite complex, including Fe-rich nodules ($Fe_{28}Cr_{17}O_{53}$ by EDX), lighter ($Mn_{25}Cr_{19}O_{55}$ by EDX) and darker ($Ti_{28}O_{72}$ by EDX) appearing areas.

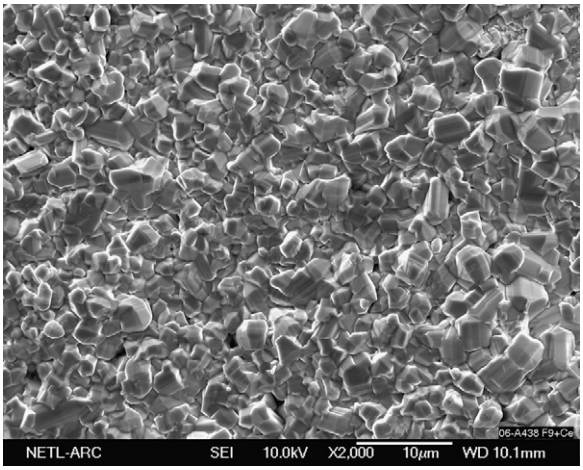

Fig. 6. An SEM micrograph of the oxide surface that formed on the surface treated F9 alloy (12Cr + CeOx) after 2000 h exposure at 800 °C in moist air. Note that the oxide scale consists of fine, equiaxed crystals.

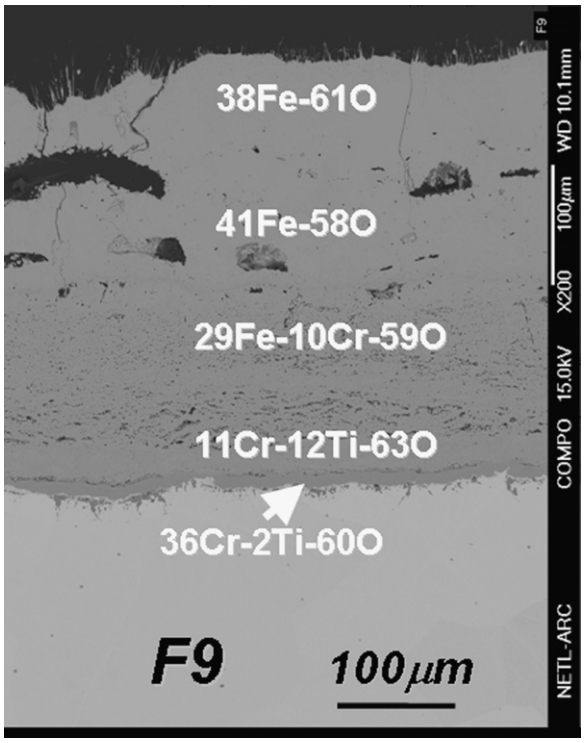

Fig. 7. An SEM micrograph of the F9 alloy (12Cr) after 2000 h exposure at 800 °C in moist air is shown in cross section at the metal/oxide interface. Note that the scale is cracked and has oxide whiskers growing from the surface.

These observations agree reasonably well with the phases identified by XRD (Table 3). The oxidized surface of the Ce treated experimental alloy with 22 wt.% Cr is shown in Fig. 10. A uniform fine grained crystalline structure was observed. The chemistry of

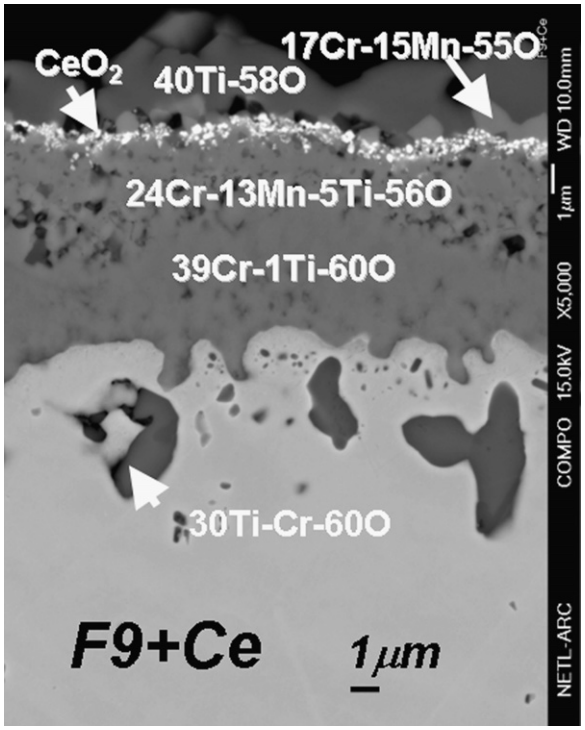

Fig. 8. An SEM micrograph of the surface treated F9 alloy (12Cr + CeOx) after 2000 h exposure at 800 °C in moist air is shown in cross section at the metal/oxide interface. Note that the scale is compact and intact.

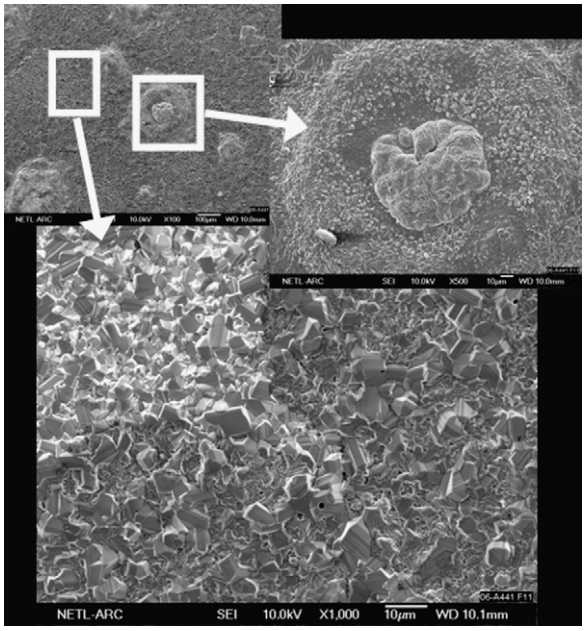

Fig. 9. An SEM micrograph of the oxide surface that formed on the F11 alloy (22Cr) after 2000 h exposure at 800 °C in moist air. Note that the nodule was found to be Fe rich while the remaining material appeared to consist of two distinct regions: $Mn_{25}Cr_{19}O_{55}$ (brighter, upper left) and $Ti_{28}O_{72}$ (darker, remaining material).

the scale was determined to be $Ti_{32}O_{68}$ and $Ti_{30}O_{70}$ which is close to the XRD determined structure of TiO_2.

Figs. 11 and 12 are SEM micrographs of cross sections of the oxide scales that formed on the experimental alloy with 22 wt.% Cr in the untreated and Ce treated conditions, respectively. Note the different magnifications. In the case of the untreated specimen (Fig. 11) a multi-layered scale was observed which consisted of Cr–Mn–Fe rich in the outer layer, Cr–Fe rich and predominantly Cr rich in the inner layers. Again, substantial titanium was only observed at the scale/metal interface of the untreated alloy. In the case of the Ce treated specimen, an overgrowth of Ti-rich oxide was observed above the residual Ce–Ox particles. The WDX chemistry of this layer was $Ti_{40}O_{58}$, reconfirming that it is not likely stoichiometric TiO_2 that is forming as the outer layer. Chrome–manganese-rich oxides were observed both under the Ti-rich layer and under the residual Ce–Ox particles. A Cr-rich scale was observed at the oxide/metal interface. Some internal oxidation (titanium) was also observed.

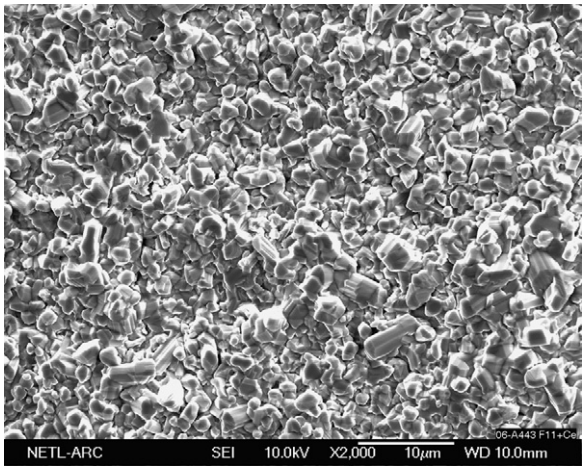

Fig. 10. An SEM micrograph of the oxide surface that formed on the surface treated F11 alloy (22Cr + CeOx) after 2000 h exposure at 800 °C in moist air. Note that the surface consisted of fine uniform oxide grains.

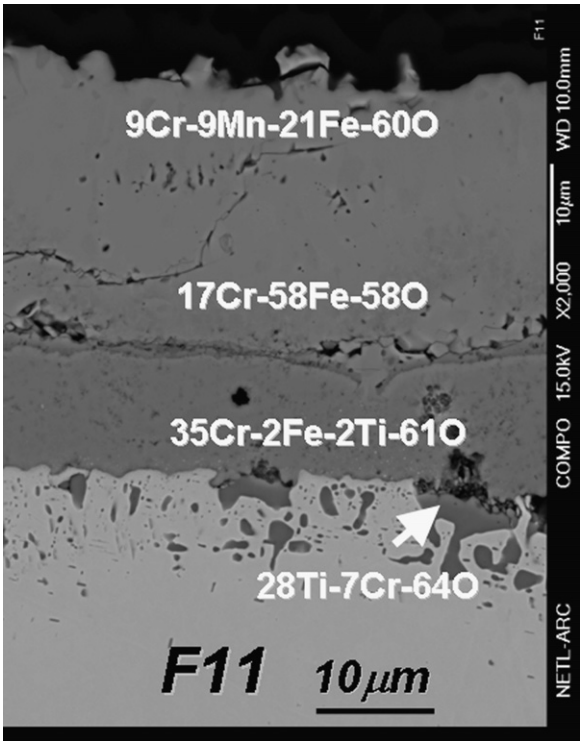

Fig. 11. An SEM micrograph of the F11 alloy (22Cr) after 2000 h exposure at 800 °C in moist air is shown in cross section at the metal/oxide interface. Note that the scale is multi-layered.

4. Discussion

The untreated experimental alloys containing 1 wt.% titanium all had high oxidation rates under the test conditions, with the possible

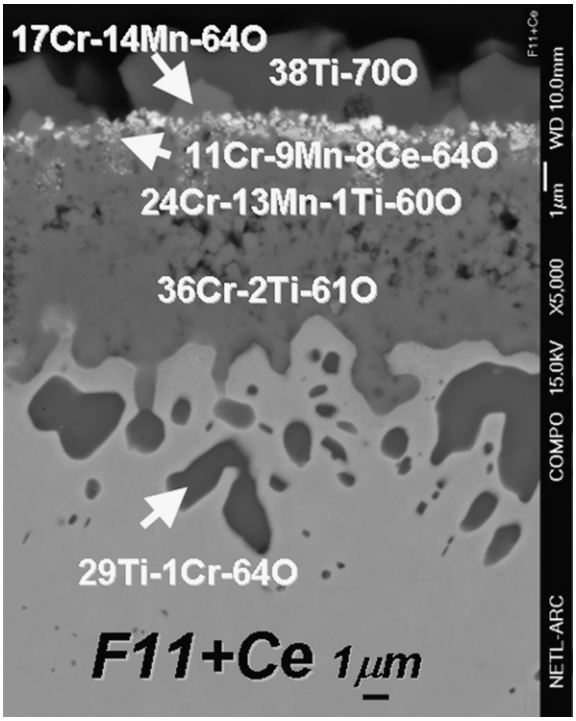

Fig. 12. An SEM micrograph of the surface treated F11 alloy (22Cr + CeOx) after 2000 h exposure at 800 °C in moist air is shown in cross section at the metal/oxide interface. Note that the scale is compact and intact.

Table 4
Driving force for the formation of the various oxides is given in the table below

Oxide	Driving force for formation at 800 °C (kJ mol^{-1})
CrO_2	241
CrO_3	204
Cr_2O_3	271
Cr_5O_{12}	231
Cr_8O_{21}	221
Cr_2FeO_4	252
FeO	187
Fe_2O_3	211
Fe_3O_4	208
$FeTiO_3$	284
Fe_2TiO_4	256
MnO	217
MnO_2	208
Mn_2O_3	221
Mn_3O_4	224
Mn_2TiO_4	276
$MnTiO_3$	298
TiO_2	343
Ti_2O_3	321
Ti_3O_5	329
Ti_4O_7	335

These driving forces in this table were calculated using Thermo-Calc using the SSOL4 and SSUB3 databases with the temperature set at 800 °C and the alloy chemistry set to that of F11.

exception of the alloy that also contained 22 wt.% Cr. These high oxidation rates can be understood from the evaluation of the oxide scale cross sections. All of the untreated alloys had complex, multi-layered oxides which were high in Fe content. Iron oxides are not considered to be protective, and are known to grow at a relatively fast rate. Cracks in the oxide scales (see Figs. 5, 7 and 11) further provide for fast pathways for oxygen ingress to the alloy surface. Although the titanium was incorporated into the oxide scale near the metal/scale interface, this Cr–Ti oxide did not appear to act as a barrier to oxide scale growth. This may be due to cracks propagating in from the thick iron-rich outer scales, or it may be due to the nature of the Cr–Ti-rich scale itself. The minor amounts of internal Ti-rich oxides were considered inconsequential to both the scale growth and weight gain.

The cerium surface treatment produced a complete change in alloy response to these test conditions. First, the oxidation rate of the experimental alloy with 22 wt.% Cr has been reduced by about a factor of nearly 3 (Fig. 3). Next, the oxidation rates of the 12, 18 and 22 wt.% Cr alloys are essentially identical (Figs. 3 and 4), thus the oxidation rates of the lower Cr alloys have been reduced from their untreated condition much more significantly than the 22 wt.% Cr alloy. This result suggests that the presence of CeO_2 significantly changes the activities of the oxidizing species and/or it significantly reduces their diffusivities. Comparing the treated vs. untreated X-ray diffraction results from the oxidized coupons (Table 3) as well as the WDX chemistries of the oxide scale cross sections (Fig. 7 vs. Fig.8 and Fig.11 vs. Fig.12), we found that the Ce treatment promoted both the formation of TiO_2 and more protective Cr-rich oxides at the exclusion of Fe containing oxides. From the cross sections of the experimental alloys with 12 and 22 wt.% Cr, we first noted that they were essentially identical in thickness and constituency. A continuous overgrowth of titanium oxide was observed to form on top of the residual CeOx left over from the treatment process. These CeOx particles act as diffusion markers which indicate the outward diffusion of Ti to form a continuous titanium oxide surface layer in the presence of CeO_2. This was completely unexpected. In commercial alloys with 0.5–1 wt.% silicon, it is common to observe a thin silica-rich layer at the metal/oxide scale interface under these experimental conditions [37,38]. We have observed that formation of a SiO_2 layer is repressed when the Ce treatment is applied to silicon containing alloys [33]. In the case of these experimental alloys however, we find that the minor element titanium is promoted to the surface to oxidize at the exclusion of the other elements. Titanium oxides have a significantly higher (more negative) ΔG of formation in comparison to the other oxidizing species that might form in this alloy series (Table 4). Thus, it is not surprising that the outer layer is essentially pure titanium oxide at the exclusion of other elements (though it remains unclear why this is not also the case in the alloys without the surface treatment). This formation of a titanium oxide layer may have several positive effects for application as an interconnect material in SOFC applications. First, the oxide scale is thin, which presumably would lead to a reduced electrical resistance. Second, since the outer layer contains no Cr, the migration of Cr to the cathode which poisons its effectiveness [21–27] would be expected to be greatly reduced if not eliminated [27–30]. Finally, the Ti-rich outer oxide that forms is expected to be electrically conductive under SOFC operating conditions [17–20].

5. Conclusions

The experimental Fe–6–22Cr–1Ti–0.5Mn alloys all formed multi-layered oxide scales under the test conditions (800 °C in air + 3% H_2O). The 6 and 9 wt.% Cr alloys both oxidized rapidly even with the Ce treatment. All of the untreated experimental alloys showed a high concentration of iron in the outer scale region which is not considered to be protective. It was observed that the Ce treatment, which incorporates Ce into the alloy surface, suppressed the formation of Fe containing oxides in the 12–22 wt.% Cr alloys. This suppression lead to the formation of more protective oxide scales. Cerium treating these experimental alloys, which contained essentially no Al or Si, but did contain 1 wt.% Ti, promoted an overgrowth of titanium oxide. This overgrowth layer does not appear to be stoichiometric TiO_2 and may prove to be an effective barrier to both scale growth and Cr vaporization. These are critical features of a successful metallic interconnect in SOFC application. In situ measurements are currently underway to evaluate the resistivity of the scale and thus evaluate the applicability of these alloys and the treatment in combination.

References

[1] Fuel Cell Handbook, EG&G Technical Services, under contract number DE-AM26-99FT40575 with US Department of Energy, Office of Fossil Energy, 7th ed., National Energy Technology Laboratory (2004) (Chapter 1).
[2] N.Q. Minh, J. Am. Ceram. Soc. 76 (3) (1993) 563–588.
[3] Fuel Cell Handbook, EG&G Technical Services, under contract number DE-AM26-99FT40575 with US Depatment of Energy, Office of Fossil Energy, 7th ed., National Energy Technology Laboratory (2004) (Chapter 7).
[4] M.C. Williams, J.P. Strakey, W.A. Surdoval, J. Power Sources 143 (2005) 101–196.
[5] M.C. Williams, J.P. Strakey, W.A. Surdoval, L.C. Wilson, Solid State Ionics 177 (2006) 2039–2044.
[6] M.C. Williams, J.P. Strakey, W.A. Surdoval, J. Power Sources 159 (2006) 1241–1247.
[7] S. de Souza, S.J. Visco, L.C. De Jonghe, Solid State Ionics 98 (1997) 57.
[8] H. Ishihara, H. Matsuda, Y. Takita, J. Am. Chem. Soc. 116 (1994) 3801.
[9] M. Feng, J.B. Goodenough, Eur. J. Solid State Inorg. Chem. T31 (1994) 663.
[10] P. Huang, A. Petric, J. Electrochem. Soc. 143 (5) (1996) 1644.
[11] K.Q. Huang, R. Tichy, J.B. Goodenough, J. Am. Ceram. Soc. 81 (1998) 2565.
[12] W.Z. Zhu, S.C. Deevi, Mat. Res. Bull. 38 (2003) 957–972.
[13] T. Horita, Y.P. Xiong, K. Yamaji, N. Sakai, H. Yokokawa, J. Power Sources 118 (2003) 35.
[14] Z. Zeng, K. Natesan, Solid State Ionics 167 (2004) 9.
[15] K. Huang, P.Y. Hou, J.B. Goodenough, Solid State Ionics 129 (2000) 237.
[16] J.W. Fergus, Mater. Sci. Eng. A397 (2005) 271.
[17] S. Geng, J. Zhu, J. Power Sources 160 (2006) 1009–1016.
[18] S.J. Geng, J.H. Zhu, Z.G. Lu, Scripta Mater. 55 (2006) 239–242.
[19] H. Nagai, K. Ohbayahi, J. Am. Ceram. Soc. 72 (1989) 400.
[20] G. Meier, SECA Annual workshop and core technology program peer review workshop, May 11–13, 2004, Boston, MA (http://www.seca.doe.gov).
[21] S.P. Simner, M.D. Anderson, G.-G. Xia, Z. Yang, L.R. Pederson, J.W. Stevenson, J. Electrochem. Soc. 152 (4) (2005) A740.

[22] M.C. Tucker, H. Kurokawa, C.P. Jacobson, L.C. De Jonghe, S.J. Visco, J. Power Sources 160 (2006) 130.
[23] M. Kumpelt, T. Kaun, T.A. Cruse, M. Hash, SECA Annual Workshop, May 11–13, 2004, available at http://www.seca.doe.gov.
[24] S.P.S. Badwal, R. Deller, K. Foger, Y. Ramprakash, J.P. Zhang, Solid State Ionics 99 (1997) 297.
[25] Y. Matsuzaki, I. Yasuda, Solid State Ionics 132 (2000) 271.
[26] S.P. Jiang, J.P. Zhand, X.G. Zheng, J. Eur. Ceram. Soc. 22 (2002) 361.
[27] Z. Yang, G. Xia, P. Singh, J.W. Stevenson, J. Power Sources 155 (2006) 246.
[28] X. Chen, P.Y. Hou, C.P. Jacobson, S.J. Visco, L.C. De Jonghe, Solid State Ionics 176 (2005) 425–433.
[29] Z. Yang, G. Xia, G. Maupin, J. Stevenson, Surf. Coat. Technol. 201 (2006) 4476–4483.
[30] Z. Yang, G. Xia, X. Li, J. Stevenson, Int. J. Hydrogen Energy 32 (2007) 3648–3654.
[31] P.D. Jablonski, D.E. Alman, Steven C. Kung, in: N. Bansal (Ed.), Ceram. Eng. Sci. Proc. 26 (4), Westerville, OH, 2005, p. 193.
[32] D.E. Alman, P.D. Jablonski, S.C. Kung, in: N.Bansal (Ed.), Ceram. Eng. Sci. Proc. 27 (4), Amer. Ceram. Soc., Westerville, OH, 2006, p. 253.
[33] D.E. Alman, P.D. Jablonski, Int. J. Hydrogen Energy 32 (2007) 793.
[34] J. Froitzheim, G.H. Meier, L. Niewolak, P.J. Ennis, H. Hattendorf, L. Singheiser, W.J. Quadakkers, J. Power Sources 178 (2008) 163–173.
[35] Z. Yang, G. Xia, C. Wang, Z. Nie, J. Templeton, J. Stevenson, P. Singh, J. Power Sources, submitted for publication.
[36] T. Horita, H. Kishimoto, K. Yamaji, Y. Xiong, N. Sakai, M.E. Brito, H. Yakokawa, J. Power Sources 176 (2008) 54–61.
[37] H.E. Evans, D.A. Hilton, R.A. Holm, Oxid. Met. 19 (1983) 1.
[38] J.S. Dunning, D.E. Alman, J.C. Rawers, Oxid. Met. 57 (2002) 409.